
Article:
Klose, Sarah Johanna, Ellis, James, Riedel, Frederik orcid.org/0000-0002-6047-262X et al. (7 more authors) (2020) The spatial distribution of hydrogen and oxygen atoms in a cold atmospheric pressure plasma jet. Plasma Sources Science and Technology. 125018. ISSN 0963-0252

https://doi.org/10.1088/1361-6595/abcc4f

The spatial distribution of hydrogen and oxygen atoms in a cold atmospheric pressure plasma jet

S-J Klose[1], J Ellis[1,2], F Riedel[2], S Schröter[2], K Niemi[2], I L Semenov[1], K-D Weltmann[1], T Gans[2], D O'Connell[2], and J H van Helden[1]

[1]Leibniz Institute for Plasma Science and Technology (INP), Felix-Hausdorff-Str. 2, D-17489 Greifswald, Germany

[2] York Plasma Institute, Department of Physics, University of York, Heslington, York, YO10 5DD, United Kingdom

E-mail: sarah-johanna.klose@inp-greifswald.de

Abstract. Cold atmospheric pressure plasma jets (CAPJs) are an emerging technology for the localised treatment of heat sensitive surfaces. Adding humidity to the CAPJ's feed gas yields an effective production of highly reactive intermediate species, such as hydrogen atoms, oxygen atoms, and hydroxyl radicals, among others, which are key species for biomedical applications. This study focusses on the effluent of the CAPJ kINPen, which was operated with argon feed gas and a humidity admixture of 3000 ppm, while a gas curtain was used to limit the diffusion of ambient air into the effluent. The axial and radial density distribution of O and H atoms is measured by means of picosecond two-photon absorption laser induced fluorescence spectroscopy (ps-TALIF). A maximum O atom density of $(3.8 \pm 0.7) \cdot 10^{15}$ cm^{-3} and a maximum H atom density of $(3.5 \pm 0.7) \cdot 10^{15}$ cm^{-3} are found at the nozzle of the plasma jet. The experimental results are compared to a two-dimensional reacting flow model that is coupled with a local zero-dimensional plasma chemical model. With this model, the main H and O atom production mechanisms are determined to be the dissociation

of H_2O and O_2 in the plasma zone of the plasma jet. The latter indicates, that a significant amount of oxygen (1%) was present inside the device. The reaction of OH with O atoms represents the main consumption pathway for O atoms and is at the same time a significant production pathway for H atoms. The main consumption of H atoms is through a three-body reaction including O_2 to form HO_2, which consumes more H and O atoms to form OH. It is pointed out, that most of the species are produced in the plasma zone, and that O and H atoms, OH and HO_2 radicals, and O_2 and H_2O molecules are strongly connected.

Keywords: Cold atmospheric pressure plasma jet, plasma medicine, spatial density, hydrogen atoms, oxygen atoms, reaction kinetics, plasma sources

1. Introduction

The introduction and development of cold atmospheric pressure plasma jets (CAPJs) has expanded the horizon for the localised treatment of heat sensitive materials, such as: the functionalisation of polymers in materials processing, wound healing of human skin and cancer research in plasma medicine, and the treatment of seeds and plants in plasma agriculture [1, 2, 3, 4, 5, 6]. CAPJs have considerable potential for biomedical applications, because they provide, besides (UV) radiation and electric fields, a large variety of reactive oxygen-nitrogen species at around room temperature [7]. One important questions, on the forefront of this research field, is how the reactive species composition can be tailored for a specific purpose [8, 9, 10].

From investigations on plasma-cell and plasma-liquid interactions it is known that water is the dominant species to initiate plasma-driven effects on cells [11, 12, 13]. When water undergoes dissociation, either within the plasma or the effluent, then intermediate species such as hydrogen atoms, H, or hydroxyl radicals, OH, are formed. These

species drive the reaction kinetics that allows the formation of more complex species, for instance, hydrogen peroxide, H_2O_2, which is a key species for the plasma-induced effects on biological tissue. H_2O_2 causes oxidative stress on cells thereby reducing the cell viability, and leads to apoptotic cell death at high concentrations [11, 14]. Another important molecule is the hydroperoxyl radical, HO_2, which can enter cell membranes and is the protonated form of the superoxide anion, O_2^-. This species is associated with the acidification of plasma-treated liquids [15]. HO_2 is formed by the reaction of H atoms with O_2 molecules, present in the atmosphere, and is involved in the reaction cycle of H_2O_2 [16]. Where the reactive species, such as H_2O_2, are produced is still an open question [11]. They may either be produced in the gas phase [14, 17], or within the liquid via secondary reactions [18]. A complete understanding of the reaction kinetics network, in both the gas and liquid phase, will help to identify the affects of certain species on biological tissue.

A quantification of the reactive species in CAPJs is challenging due to the small diameter, which is usually in the order of mm. One diagnostic technique that is commonly used to measure atomic and molecular radicals is absorption spectroscopy [19]. However, due to the large energy gap between ground and excited states, the investigation of atomic ground state densities requires light sources in the vacuum ultra-violet (VUV) region, where light is strongly absorbed by air. Previously, O and N atoms have been quantified in a CAPJ, operating in helium, using synchrotron radiation and a spectrometer with an ultra-high spectral resolution, so-called VUV high-resolution Fourier-Transform Absorption Spectroscopy (VUV-FTAS) [20, 21]. Another, more common approach is two-photon absorption laser induced fluorescence spectroscopy (TALIF) [22], which has been applied previously to determine H and O atom densities in CAPJs [23, 24, 25, 26]. A reliable result for the atomic density can only be obtained

by taking into account the non-radiative losses of the excited state population by collisional quenching, as this, at atmospheric pressure, usually dominates over the spontaneous emission. To calculate the total quenching loss, a detailed knowledge of the gas composition and the specific quenching rate coefficients is required.

Recently, Schröter et al. [27] reported H atom density measurements in the effluent of a CAPJ, operating with humidified He, which have been obtained with a picosecond TALIF laser and imaging system. The picosecond time resolution allows an independent and direct measurement of the effective (reduced) lifetime of the excited state. Absolute number densities are determined from comparative TALIF measurements at known densities of a noble gas, e.g. krypton for H atoms [28], and xenon for O atoms [29].

In this work, the spatial density distributions of O and H atoms in the effluent of the kINPen-sci plasma jet, which was operated with humidified Ar feed gas, is obtained by picosecond TALIF. The experimental results are compared to density distributions determined by a two-dimensional reacting flow model that is coupled with a local zero-dimensional plasma chemical model for describing the generation of the primary reactive gas species. The dominant formation and destruction pathways for O and H atoms are identified. It was observed that even a small amount (about 1%) of O_2 in the plasma zone has a strong influence on the reactive species composition in the effluent.

The paper is structured as follows: In section 2, the plasma jet and the experimental setup are described. In section 3, the calibration procedure to obtain absolute number densities from TALIF measurements is outlined. In section 4, a brief description of the plasma chemical and reacting flow model is provided. In section 5, spatial distributions of O and H atoms are presented and compared to densities obtained from the model. In section 6, the work is summarized.

2. Experimental setup

2.1. Plasma jet

The investigated kINPen-sci plasma source is a cold atmospheric pressure plasma jet device, that consists of a dielectric capillary with a diameter of 1.6 mm, in which the plasma is ignited between a powered inner needle electrode (frequency $\approx$ 1 MHz, power = 1−3 W) and a grounded outer ring-electrode [30, 31]. A total flow of 3 slm Ar was used as the feed gas, with 10% of this being guided through a bubbler with distilled water at room temperature, which ensures a content of 3000 ppm humidity at full water vapour saturation. Additionally, the kINPen-sci was operated with a gas curtain that provides a concentric gas flow, that shields the plasma effluent from the influx of surrounding ambient air. The composition of the gas curtain can be varied from pure nitrogen to pure oxygen at a total flow rate of 5 slm [32].

2.2. Picosecond two-photon absorption laser induced fluorescence spectroscopy

The experimental setup for picosecond TALIF is schematically shown in Figure 1 and described in detail previously [27].

The laser system (EKSPLA) is based on a Nd:YAG pump laser (1064 nm) with a mode-locked oscillator, a regenerative amplifier, and a single pulse power amplifier, producing a weak pulse train output and a strong single pulse output with a single pulse duration of 30 ps. In the second laser unit the weak train beam is amplified and frequency-tripled (355 nm), the strong single pulse beam is frequency-tripled only, while the left-over of the 1064 nm single pulse is the third output beam. In the third laser unit the 355 nm train enters an optical parametric oscillator (OPO) state providing tunable but weak radiation between 420 to 710 nm, that is amplified using the strong 355 nm single pulse in a subsequent optical parametric amplifier (OPA) stage. Subsequent

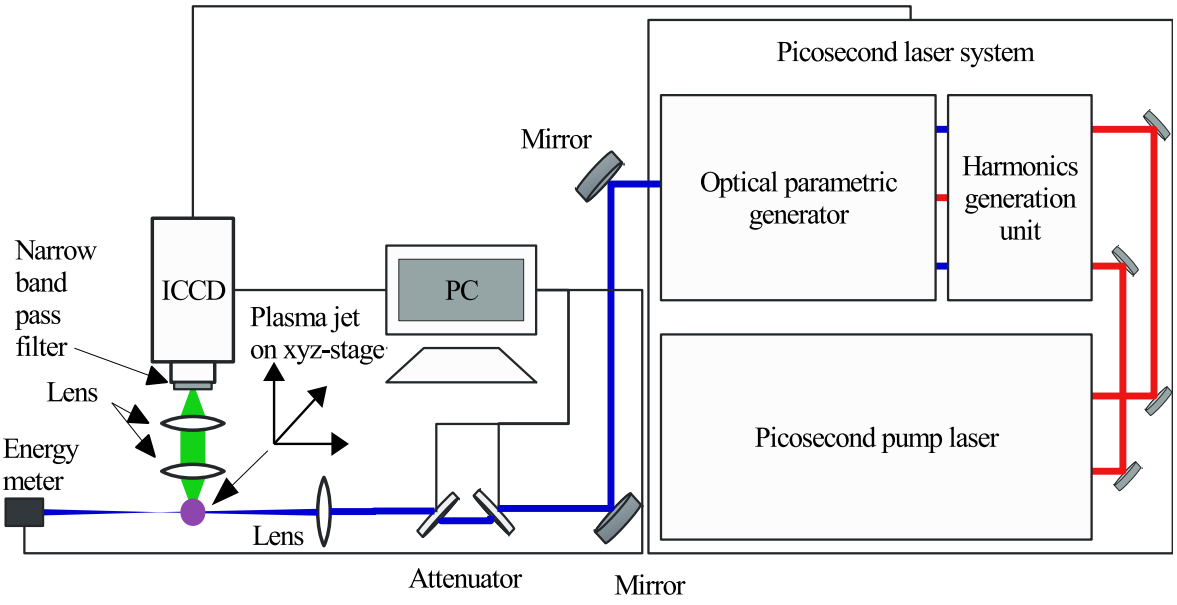

Figure 1: Schematic of the experimental setup illustrating the three units of the picosecond laser system, the UV output beam attenuated and focussed into the effluent of the kINPen-sci, which was mounted vertically on an xyz-translation stage, and the VIS/NIR detection system (lens doublet, interference filter, and camera) perpendicular to the laser beam.

frequency-doubling is used to generate the UV wavelengths between 210 to 355 nm, and additional sum-frequency mixing with the left-over 1064 nm single pulse input for the deep UV wavelengths below 210 nm. In the UV range, 30 ps laser pulses were generated, with a pulse energy of a few hundred μJ at the maximum, and a spectral width of approximately 4 cm^{-1}. The applied laser pulse energy was measured behind the laser focus/plasma interaction volume with a pyroeletric detector (Gentec-EO, QE8SP-B-MT) and controlled with the help of an attenuator-compensator system, which comprises two specifically coated counter-rotating CaF_2 substrates that are actuated by a stepper motor. The standard deviation of the shot-to-shot fluctuations in the pulse energy is approximately 8%. The laser beam was focussed by a spherical plano-convex fused-silica lens, with a focal length of 30 cm, in a plane approximately 1 cm behind the plasma jet. This was conducted to widen this interaction zone of the laser beam with the species

under investigation, to avoid saturation of the two-photon transitions, and to mitigate material damage in the calibration cuvettes. The fluorescence signal of the excited states was detected perpendicular to the direction of the laser beam by using an intensified charge coupled device camera (iCCD: Stanford Computer Optics, 4Picos dig), after passing two achromatic lenses (Thorlabs, AC050-010-B-ML, focal length: 80 mm) and an interference filter (central wavelengths $\lambda_O = 845$ nm, $\lambda_H = 656$ nm, $\lambda_{Xe} = 835$ nm, $\lambda_{Kr} = 825$ nm, band width $\Delta\lambda = 10$ nm). This allowed the complete region of interest to be imaged and reduced the detection of broad band plasma emission. In order to synchronize the laser pulse with the acquisition by the iCCD camera, the pre-trigger output of the mode-locked pump laser was used. For all TALIF measurements, the laser pulse energy was reduced sufficiently to ensure the unsaturated quadratic signal dependency. In Table 1, the observed states, their natural lifetimes, optical branching ratios, excitation wavelengths, the applied laser pulse energies, and the band pass filters used for selecting the fluorescence wavelengths are summarised.

The plasma jet was placed on a motorised xyz translation stage (Zaber). In the following, the z-axis is defined as the axis along the symmetry axis of the effluent through the centre of the plasma jet nozzle, the x-axis is the axis parallel to the laser beam, which crosses the centre of the nozzle.

Table 1: Analysed species with natural lifetime τ_{nat}, taking fine structure splitting into account, optical branching ratio $b_{ik,nat}$, two-photon excitation wavelength λ_l, applied laser pulse energy E_l and the filters used to detect the fluorescence.

Species (excited state)	τ_{nat} [ns]	$b_{ik,nat}$	λ_l [nm]	E_l [μJ]	Filter [nm]
H(3d ^{2}D$_J$)	17.6	1	205.11	35	656±5
Kr(5p′[3/2]$_2$)	34.1	0.958	204.13	0.28	825±5
O(3p ^{3}P$_J$)	34.7	1	225.64	40	845±5
Xe(6p′[3/2]$_2$)	40.8	0.733	224.31	0.45	835±5

3. Obtaining absolute number densities

In order to determine absolute number densities from the fluorescence signal, a calibration procedure needs to be employed; the fluorescence signal of the species of interest is compared to the fluorescence signal of a suitable reference gas. Relevant for this calibration is the measurement of the fluorescence signal, both spectrally and temporally integrated, as well as the effective lifetime of the upper state. Throughout the remainder of this work, the spatially, spectrally, and temporally integrated fluorescence signal is denoted as the total TALIF signal. A detailed mathematical description of the calibration procedure and the unsaturated TALIF signal dependency can be found in [33]. In this work, a quartz glass cuvette with a gas filling of either 10 Torr Xe or 1 Torr Kr was used. The corresponding absorption cross section ratios were $\frac{\sigma_O}{\sigma_{Xe}} = 1.90 \pm 0.38$ [29] and $\frac{\sigma_H}{\sigma_{Kr}} = 0.62 \pm 0.31$ [28], respectively.

In Figure 2a, an overlay of several camera images are shown: A shadow image of the plasma jet nozzle, and the on-resonance TALIF signal for O atoms at $\lambda_l(O) = 225.64$ nm as measured at various distances z from the plasma jet's nozzle. In Figure 2b, the equivalent for the TALIF signal for H atoms at $\lambda_l(H) = 205.11$ nm is presented. Each TALIF signal measurement results from an average of 64 or 256 accumulations (number of laser shots) with a camera gate width of 120 ns, which is sufficiently large to capture the entirety of the fluorescence decay. The accumulated background signal from the camera and the optical plasma emission as measured off-resonance was subtracted accordingly. It was observed that more accumulations were necessary in the instance of the O atom measurements (256) compared to the H atom measurements (64). This was required in order to obtain a comparable signal-to-noise ratio, most likely as a result of the delicate nature of the laser's wavelength dependency. The shadow image of the plasma jet was taken by using an LED for back illumination. By using the nozzle

diameter of 2.4 mm as a reference, the scaling of the image in terms of mm length per pixel was determined.

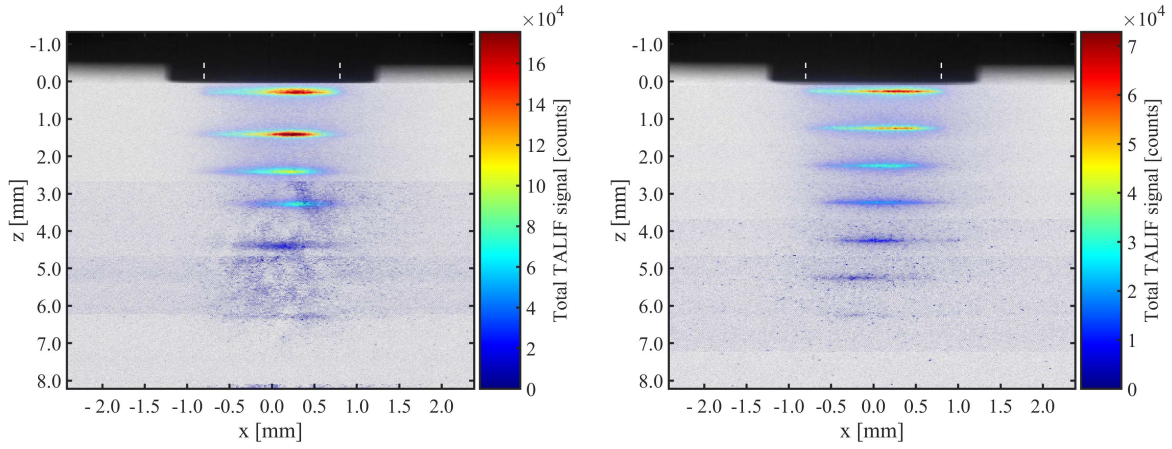

Figure 2: Overlaid images of the on-resonance fluorescence signal as measured at various distances z to the nozzle together with a shadow image of the nozzle: a) O atoms, $\lambda_l(O) = 225.64$ nm, 256 accumulations; b) H atoms, $\lambda_l(H) = 205.11$ nm, 64 accumulations.

TALIF spectra of the two-photon resonances were obtained by measuring the fluorescence signals within a region of interest on the camera chip as a function of the laser wavelength. By subdividing the interaction zone of the laser beam with the plasma effluent into frames of 4×8 pixels (50×100 μm) in x and z direction, over which the signal was accumulated, spatial resolution was achieved. In Figure 3, a measured example spectrum of the two photon excitation from the lowest component of the ground state of O ($2p_4^3P_{J=2}$) to the three close-by components of the upper state ($3p^3P_{J=1,2,0}$), accumulated over the entire region of the fluorescence signal, is shown at $z = 0.25$ mm together with a best fit of a Gaussian function (FWHM$= 16.6 \pm 1.3$ pm).

Unfortunately, the spectral resolution of the picosecond laser system of approximately 4 cm^{-1} is insufficient to resolve the O($3p^3P_{J=1,2,0}$) fine structure of the upper level ($\approx$ 0.7 cm^{-1}), nor to determine reliable values for the Doppler width and pressure

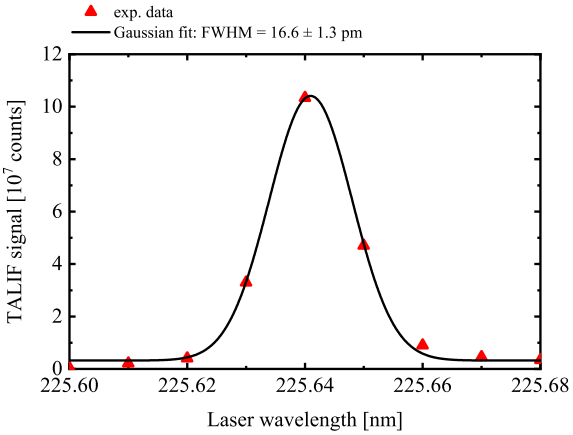

Figure 3: TALIF spectrum for the O $2p_4^3P_{J=2} \rightarrow 3p^3P_{J=1,2,0}$ transition determined at $z = 0.25$ mm, together with a Gaussian fit. Each data point was obtained by accumulating the entirety of the fluorescence signals of 256 laser shots with a camera gate width of 120 ns.

broadening under the investigated conditions, which in contrast is possible with a conventional nanosecond TALIF laser system, e.g. see ref. [29]. In this work, the spectral profile of the TALIF measurements comprises of 6 data points, with a wavelength interval of 0.01 nm, that enables a Gaussian profile to be fitted. The area of this Gaussian profile is the total TALIF signal that is used for the calculation of ground state densities.

Considering collisional quenching, the natural branching ratio $b_{ik,nat} = \frac{A_{ik}}{A_i}$ is reduced to the effective branching ratio b_{ik}, which is given by:

$$b_{ik} = \frac{A_{ik}}{A_i + \sum_q k_{i,q} n_q} = b_{ik,nat} \frac{\tau_{eff}}{\tau_{nat}}. \quad (1)$$

Here, A_{ik} is the Einstein coefficient for spontaneous emission from the excited state i to a lower state k, and τ_{nat} is the natural lifetime of the state i as the inverse of the total spontaneous emission rate $A_i = \sum_j A_{ij}$ to all possible lower states j. k_i are the quenching coefficients for all the quenching species q, with density n_q, and τ_{eff} is the effective lifetime, which is the lifetime of the exited state reduced by collisional quenching.

The effective lifetimes of the excited states were determined from the measured temporal decay of the fluorescence signal. At on-resonance laser wavelength, the delay between laser pulse and camera trigger was varied in equidistant steps, while keeping the camera gate width constant. For the slower TALIF decay of O atoms a time increment of 0.5 ns and a camera gate of 5 ns was chosen, while for the faster TALIF decay of H atoms a time increment of 50 ps, and a gate width of 800 ps was used. The oversampling is necessary to obtain a signal-to-noise ratio above the detection limit. In Figure 4, an example of the measured TALIF signal for O atoms at $z = 0.25$ mm is shown as a function of time, where the black solid curve represent the best fit by a purely exponential decay after the laser excitation. The effective lifetime was determined for each measurement from the decay time of the exponential fit. At $z = 0.25$ mm, for instance, an effective lifetime

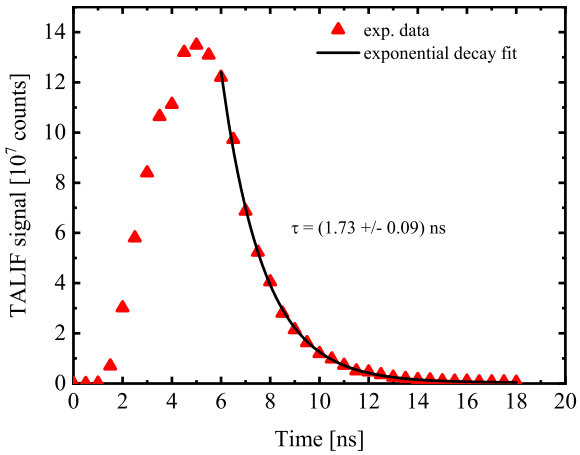

Figure 4: Time resolved O($3p^3P_J$) TALIF signal at $z = 0.25$ mm obtained with 0.5 ns time steps and 5 ns camera gate width.

of $\tau_{eff} = (1.7 \pm 0.1)$ ns was observed for O atoms. The measured effective lifetime is slightly lower than the calculated effective lifetime $\tau_{eff}^{theo} = 2.21 \pm 0.10$ ns (see Equation 1) for a gas mixture of 3 slm Ar, at 300 K, mixed with 3000 ppm water, and quenching coefficients $k_{Ar}^{O} = (0.140 \pm 0.007) \cdot 10^{-10}$ cm^3/s [29] for excited O atoms quenched by Ar and $k_{H_2O}^{O} = (11.0 \pm 1.1) \cdot 10^{-10}$ cm^3/s [27] for excited O atoms quenched by water. This shows that additional quenching species need to be considered to match the theoretical

value to the experimental one, which will be discussed in section 5 in more detail. However, for the excited atomic hydrogen state the situation is different. Schmidt and Bittner reported quenching coefficients $k_{Ar}^{H} = (4.15 \pm 0.03) \cdot 10^{-10}$ cm^3/s in the presence of Ar [34] and $k_{H_2O}^{H} = (110 \pm 10) \cdot 10^{-10}$ cm^3/s in the presence of water [35]. The corresponding quenching rate turns out to be a factor of about 20 higher than for the atomic oxygen state: $\tau_{eff} = 90 \pm 14$ ps, using the aforementioned quenching coefficients. This value is close to the detection limit of the system of about 100 ps. Hence, the effective lifetime for excited H atoms could not be determined experimentally and the calculated value was used instead in order to give an estimation for the H atom density. A detailed description of the uncertainty analysis for the density measurements can be found in [27, 36]. The error bars shown in the following comprise the total stochastic uncertainty of about 28% for the O atom density and approximately 31% for the H atom density. They include 10% uncertainty for the laser pulse energy, 8% for the Gaussian fit, and the error of the effective lifetimes (5% for O, 7% for Xe, 4% for Kr and 15% for H). However, for the total error of the absolute number density, the uncertainty of the two-photon absorption cross section plays an important role. Therefore, systematic errors given in [27] are used for the transmission of the calibration cuvette (3%), the natural lifetimes (5% for O and Xe and 10% for H and Kr), and the two-photon absorption cross section ratios (20% for Xe-O [29] and 50% for Kr-H [28]) to determine the absolute error of the number densities, which amounts to 35% for O atoms and 61% for H atoms.

4. Plasma chemical and reacting flow model

In order to identify the most dominant reaction pathways, the experimental results were compared with species densities obtained from numerical simulations. These were performed by using a two-dimensional axisymmetric model of the turbulent reacting

flow coupled with a local zero-dimensional plasma chemical model for the kINPen-sci plasma jet, reported by Semenov et al. [37]. The model describes the formation and transport of chemically reactive species in the plasma zone and the effluent of the jet, whereas the plasma zone is characterised by a local zero-dimensional model, and the gas flow and transport of reactive species are calculated by solving the boundary-layer form of the Navier-Stokes equations.

In the present study, the following species are taken into account: Electrons (e), ground state argon atoms (Ar), metastables of argon (Ar^*) in the $Ar^3P_{2,0}$ state, argon excimers (Ar_2^*) in the $Ar_2^3\Sigma_u^+$ state, argon cations (Ar^+), diargon cations (Ar_2^+), ground state nitrogen molecules (N_2), ground state oxygen molecules (O_2), water molecules (H_2O), electronically excited nitrogen molecules (N_2^*) in the $N_2A^3\Sigma_u^+$ state, electronically excited oxygen molecules (O_2^*) in the $O_2a^1\Delta_g$ state, oxygen atoms (O), nitrogen atoms (N), hydrogen atoms (H), ground state hydroxyl radicals (OH), vibrationally excited hydroxyl radicals in the first two vibration levels ($OH_{v=1}^*$ and $OH_{v=2}^*$), hydrogen molecules (H_2), hydroperoxyl radicals (HO_2), hydrogen peroxide (H_2O_2), ozone (O_3), nitrogen monoxide (NO), nitrogen dioxide (NO_2), nitrate (NO_3), nitroxyl (HNO), nitrous acid (HNO_2), and nitric acid (HNO_3).

The governing equations of the model are solved in cylindrical coordinates (r, z), where the z-axis runs along the axis of the jet and r is the radial distance. The species mass fractions, ω_α, are determined by:

$$\rho\frac{d\omega_\alpha}{dt} = \frac{1}{r}\frac{\partial}{\partial r}\left(r\rho D_\alpha\frac{\partial\omega_\alpha}{\partial r}\right) + m_\alpha\left(G_\alpha + R_\alpha\right). \tag{2}$$

Here, α stands for the type of species, d/dt is the substantial derivative, ρ is the gas density, m_α is the mass, D_α is the diffusion coefficient, and G_α and R_α are the chemical source terms respectively, which represent the contribution of different chemical reactions.

Table 2: List of reactions used in the plasma chemical model.

Nr.	Reaction[a]	Rate coefficient[b]	References
E1	$e + Ar \rightarrow e + e + Ar^+$	BOLSIG+	[38][c]
E2	$Ar^+ + Ar + M \rightarrow Ar_2^+ + M$	2.5×10^{-31}	[39]
E3	$e + Ar_2^+ \rightarrow Ar + Ar$	$5.38 \times 10^{-8}\, T_e^{-0.66}$	[40][d]
E4	$e + Ar \rightarrow e + Ar^*$	BOLSIG+	[38][c]
E5	$Ar^* + Ar + M \rightarrow Ar_2^* + M$	2.8×10^{-33}	[41]
E6	$Ar_2^* \rightarrow Ar + Ar$	3.5×10^{5}	[41]
E7	$Ar_2^* + Ar \rightarrow Ar + Ar + Ar$	1.0×10^{-14}	[42][e]
E8	$Ar^* + O_2 \rightarrow Ar + O + O$	2.1×10^{-10}	[43]
E9	$Ar^* + N_2 \rightarrow Ar + N + N$	1.8×10^{-11}	[43][f]
E10	$Ar^* + N_2 \rightarrow Ar + N_2^*$	1.8×10^{-11}	[43][f]
E11	$Ar^* + H_2O \rightarrow Ar + H + OH$	7.8×10^{-10}	[44]
E12	$Ar_2^* + O_2 \rightarrow Ar + Ar + O + O$	4.6×10^{-11}	[45]
E13	$Ar_2^* + N_2 \rightarrow Ar + Ar + N + N$	6.0×10^{-12}	[42][f]
E14	$Ar_2^* + N_2 \rightarrow Ar + Ar + N_2^*$	6.0×10^{-12}	[42][f]
E15	$Ar_2^* + H_2O \rightarrow Ar + Ar + OH + H$	7.8×10^{-10}	[44]

[a] M denotes a third body (the concentration of M is $2.44 \times 10^{19}\,\mathrm{cm}^{-3}$).

[b] The units of rate coefficients are s^{-1}, $\mathrm{cm}^3\,\mathrm{s}^{-1}$, $\mathrm{cm}^6\,\mathrm{s}^{-1}$ for the first, second and third order reactions, respectively. The electron temperature is in units of eV.

[c] The reaction rates were computed as functions of T_e using the BOLSIG+ code [38]. The details of the computations are given in ref. [37].

[d] Reaction yields the excited Ar atom, which sequentially decays to the ground state.

[e] Reaction yields $Ar_2(^1\Sigma_u^+)$, which then dissociates into Ar atoms.

[f] Quenching rates of Ar^* ($3.6 \times 10^{-11}\,\mathrm{cm}^3\,\mathrm{s}^{-1}$) and Ar_2^* ($1.2 \times 10^{-11}\,\mathrm{cm}^3\,\mathrm{s}^{-1}$) by N_2 are branched for the formation of N and N_2^*

The substantial derivative is given by:

$$d/dt = \partial/\partial t + u\,\partial/\partial z + v\,\partial/\partial r. \quad (3)$$

Here, t is time, u and v are the axial and radial gas velocities, respectively. The velocity field and diffusion coefficient in Equation (2) are obtained by solving the corresponding flow problem in the plasma zone and the effluent [37].

G_α are the rates for the plasma induced chemical reactions summarised in Table 2 that describe the formation of primary reactive species (N, O, H, OH, N_2^*) due to dissociation and excitation of N_2, O_2, and H_2O. The spatio-temporal dependence of the production and loss rates is given by the simplified model:

$$G_\alpha(t, r, z) = G_\alpha(t, 0, z) \exp[-(r/r_0)^2]. \tag{4}$$

Here, r_0 is the characteristic radius of the power deposition profile in the jet, which describes the characteristic radius of the ionization wave propagating along the jet axis. The radius r_0 is estimated to be $0.1-0.5$ mm according to the data presented in [46, 47]. The production terms $G_\alpha(t, 0, z)$ are defined by using a local zero-dimensional plasma chemical model described in detail in [37]. With this local zero-dimensional model, mass balance equations for the species concentrations and energy balance equations for the electron temperature are solved. The heating of electrons is modelled by prescribing the source of the power density, $Q(t, z)$, in the energy balance equation. The spatio-temporal dependence of $Q(t, z)$ is given by:

$$Q(t, z) = Q_t(t)Q_z(z). \tag{5}$$

Here, $Q_t(t)$ simulates the heating of electrons in the ionization wave and is described by a periodic rectangular pulse with an amplitude of Q_0 and width τ. The repetition rate is set to 1 MHz, which is equal to the frequency of the plasma jet. The axial profile of the power density, Q_z, is taken as constant inside the plasma zone and is given for the effluent by:

$$Q_z = \exp[-(z/z_0)^2]. \tag{6}$$

Here, z_0 is the characteristic length of the power density decay. The profile Q_z is chosen mainly by analogy with that used in [48], where a similar electrode configuration to that of the kINPen-sci plasma jet was considered.

R_α are the rates for the reactions listed in Table 3, which are calculated from the product of the reagents, the rate coefficient given in the third column of Table 3, and the corresponding stoichiometric coefficient.

All the densities given by the plasma chemical and reacting flow model are periodic steady-state solutions. Further details about the model and its numerical implementation can be found in [37].

5. Results and discussion

In Figure 5, radial density profiles (lateral direction x) for O and H atoms are depicted as measured at different distances z from the jet's nozzle, while a gas curtain of oxygen-only was applied. The shown error bars comprise the stochastic uncertainties only, excluding the systematic ones (see section 3).

The atomic O and H densities were found to be distributed within the 2 mm diameter of the nozzle opening. They have similar distributions and decrease with increasing distance to the nozzle. The maximum is shifted to the right (between $x = 0.0$ mm and $x = 0.5$ mm) for the O atom density and moving from the right to the centre for the H atom density further away from the nozzle, which is also shown in Figures 2a and 2b. The lateral O atom density distributions exhibit an asymmetry, particularly at short distances from the nozzle. For example, at $z = 0.25$ mm, the O atom density is about $3.8 \cdot 10^{15}$ cm^{-3} for positive x values up to +0.5 mm, while much lower for the corresponding negative x values. Due to the lower number of accumulations of

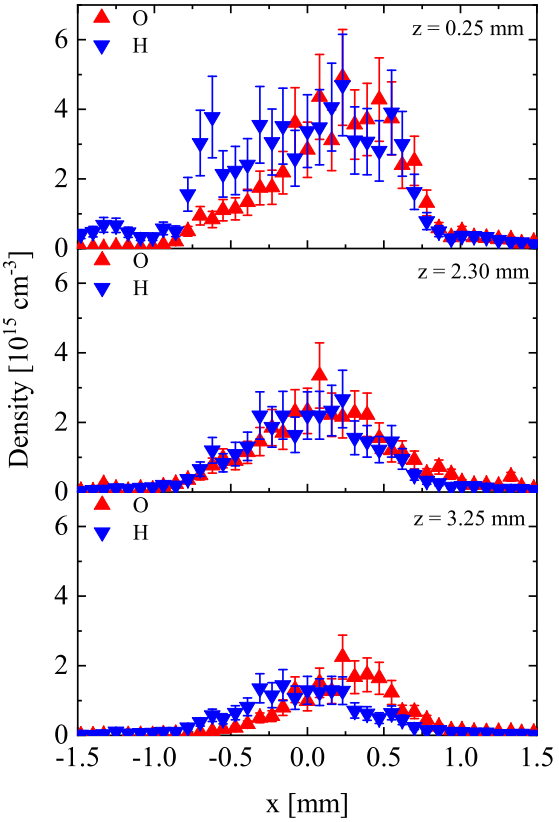

Figure 5: Density of O and H as a function of x at various z-positions with a gas curtain of 100% oxygen.

the H measurements, the H atom densities exhibit more scattering than the O density; nonetheless, an asymmetric distribution was observed, in particular, at z=0.25 mm. These distributions can be explained by the filamentary character of the plasma jet: Guided streamers are propagating into the effluent, whose directions are determined by the turbulent nature of the plasma jet resulting in an erratic path way. Close to the nozzle, the atomic densities are produced by reactions in the plasma zone of the jet, which are determined by filaments from the tip of the inner needle electrode to the outer ring-electrode. Within the plasma zone, one direction for the filament could be preferred due to inhomogeneities at the electrodes, which would result in an asymmetric production of H and O atoms due to the dissociation of H_2O and other molecular species. A similar, asymmetric distribution has also been reported previously for the density

distribution of HO_2 [63].

The averaged density values between $x = 0.0$ mm and $x = 0.5$ mm, at $z = 0.25$ mm, were similar with $3.8{\cdot}10^{15}$ cm^{-3} and $3.5{\cdot}10^{15}$ cm^{-3} for O and H respectively. Considering water as the only source for atomic oxygen and atomic hydrogen, one would expect a much lower O atom density. Whereas, atomic H is a direct dissociation product of water, secondary reactions, such as the recombination of two OH radicals, are necessary to form atomic O. However, since the plasma jet is turbulent and was operated with molecular oxygen as a curtain gas, there could have been diffusion of molecular oxygen into the effluent leading to dissociative formation of O.

In order to confirm that the dissociation of H_2O in the feed gas and the dissociation of diffused gas from the gas curtain into the effluent can not explain the O atom densities at short distances to the nozzle, the O atom density was determined by using 3 slm dry Ar as a feed gas, while varying the gas curtain composition. In Figure 6, the obtained O atom densities at $z = 1$ mm, are depicted as a function of the oxygen fraction in the gas curtain. The densities resulted from averaging between $x = 0.0$ mm and $x = 0.5$ mm, and are shown together with the corresponding standard deviation.

The O atom density results exhibit a larger error bar compared to the measurements

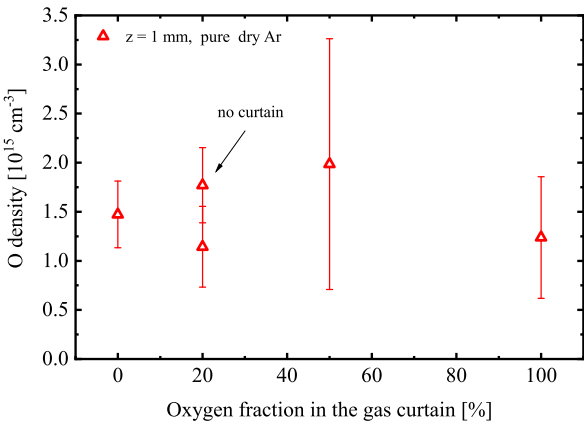

Figure 6: Measured O atom density at $z = 1$ mm with dry argon feed gas as a function of the oxygen content in the O_2/N_2 gas curtain.

with humidity. This is likely due to several optical emission lines of argon within the spectral bandpass of the used interference filter (840 to 850 nm). Since these excited argon levels are quenched less in the absence of water, a decrease in the overall signal to noise ratio is expected. Taking the error into account, the O atom density is constant at about $1.5 \cdot 10^{15}$ cm^{-3} for all gas curtain compositions. Even without a gas curtain, the atomic O density has the same value within the error. These findings are in accordance with gas flow simulations [64], mass spectrometry investigations [65], and measurements by Reuter et al. [25], who reported that the influx from the gas curtain starts to be efficient at distances beyond 4 mm from the nozzle. Moreover, the atomic H and O densities closer to the nozzle at $z = 0.25$ mm, obtained with 3000 ppm feed gas humidity, were independent from the gas curtain compositions. This demonstrates, that water present in the feed gas and species present in the gas curtain are not the origin of the measured O atoms, and that another source for oxygen needs to be present already in the plasma zone.

The kINPen-sci plasma jet was investigated to ascertain whether oxygen impurities as a result of the design of the inner gas connections may be the origin of the high O atom density. A high-precision oxygen analyser (zirconia measurement cell, Zirox) was used to the determine the molecular oxygen concentration in the feed gas without switching the plasma on. Oxygen concentrations of approximately 20 ppm for dry Ar and humidified Ar (3000 ppm) were obtained. This is a factor of three lower than the previously measured atomic O density in the absence of humidity to the feed gas.

Another explanation could be given by observing the discharge dynamics of the plasma jet. Schmidt-Bleker et al. reported a backwards directed excitation wave (towards the inside of the plasma zone) in the positive half wave of the applied voltage for a pure oxygen gas curtain and dry feed gas in a helium operated plasma jet [66]. The speed of

this backwards directed wave was two orders of magnitude higher than the gas flow of 25 m/s. Reuter et al. observed a similar feature for the same plasma jet operated with argon [67]. With such a backwards directed excitation wave, negative oxygen ions could have been drifted into the plasma zone serving as a source for atomic O.

In order to determine the amount of initial O_2 that would have been necessary in the plasma zone to explain the obtained O and H atom densities, and to identify the most important reaction pathways, the experimental results were compared with predictions from a two-dimensional reacting flow model that was coupled with a local zero-dimensional plasma chemical model. In Figure 7, contour plots for the spatial distributions of O and H atoms are illustrated as a function of the radial distance from the centre of the nozzle x and the axial distance from the nozzle z for 3000 ppm water in the Ar feed gas and a gas curtain of 100% oxygen, obtained from an interpolation between the experimental data points (Figure 7a and 7c), and from a plasma chemical and reacting flow model with 1% O_2 impurities in the feed gas (Figure 7b and 7d). In order to fill the regular grid of the contour plot, the densities measured at $z = 0.25$ mm were interpolated to $z = 0$ mm, while averaging and interpolation was performed for z-distances further from the nozzle. The model was evaluated for a feed gas composition of 3 slm Ar, 3000 ppm of water, and with 1% admixture of O_2, which was adjusted to best-fit the measured O and H atom densities. The other simulation input parameters were: Initial power density input $Q_0 = 120$ kW cm^{-3}, filament duration $\tau = 50$ ns, radius for the streamer head $r_0 = 0.35$ mm, and characteristic length for the power density decay $z_0 = 2.35$ mm.

The measured O and H atom densities are found to be distributed over the complete diameter of the nozzle, while the simulated densities are limited by the assumption that the excitation wave propagates only in a narrow radial range of $r = 0.35$ mm along the

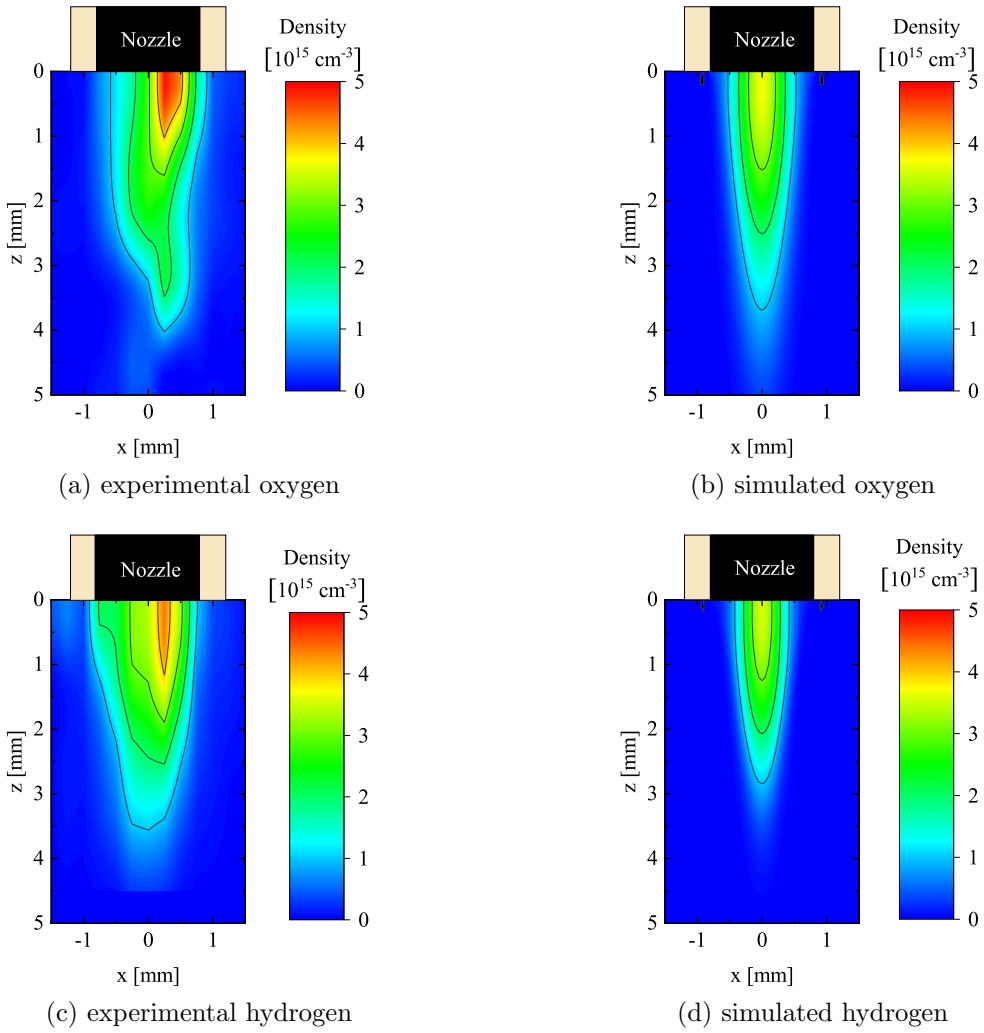

(a) experimental oxygen (b) simulated oxygen

(c) experimental hydrogen (d) simulated hydrogen

Figure 7: Spatial density distributions of O and H atoms as a function of the radial distance from the centre of the nozzle x and the axial distance from the nozzle z for 3000 ppm water in the Ar feed gas and a gas curtain of 100% oxygen, obtained from an interpolation between the experimental data points ((a) and (c)) and from a plasma chemical and reacting flow model with 1% O_2 impurities in the feed gas ((b) and (d)).

symmetry axis of the plasma jet. However, observations have shown that the excitation wave changes its direction due to inhomogeneities at the needle electrode and due to the turbulent gas flow [64]. TALIF utilises an accumulation of millions of single excitation waves, that could explain the broader distributions obtained by the experiments. In the simulation, the atomic densities of O and H are decreasing to a value below the experimental detection limit in a shorter distance than observed in the experiments.

If the errorbars for the experimental values are taken into account, the experimental values are in agreement with the simulation. However, some species within the chemical reaction scheme were not experimentally determined yet (e.g. OH), and their impact on the H and O atomic densities might be over- or underestimated in the model.

In order to identify the most dominant production and consumption mechanisms, the axial dependence of the simulated O and H atom densities was compared with the measured one, as averaged between $x = 0.0$ mm and $x = 0.5$ mm. In Figure 8, the resulting axial density profiles are shown. The experimental data agrees well with the

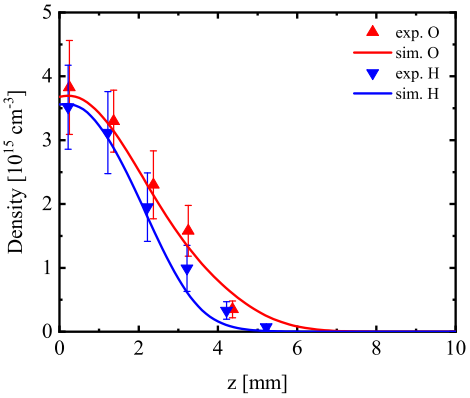

Figure 8: Axial density of O and H atoms as a function of the axial distance z to the nozzle, obtained experimentally and by numerical simulations

values determined by the plasma chemical and reacting flow model, when 1% of O_2 was added to the humid argon feed gas in the simulation.

Without the initial O_2 density, the O atom density would have been orders of magnitude lower than the H density. However, a maximum H density of $(3.5 \pm 0.7) \cdot 10^{15}$ cm^{-3}, and a maximum O atom density of $(3.8 \pm 0.7) \cdot 10^{15}$ cm^{-3} was obtained at $z = 0.25$ mm, where the error is the standard deviation within the averaged region. Interestingly, the density values of O atoms are in remarkably good agreement with the values obtained from TALIF measurements reported by Reuter et al. [25], where the O atom density in 5 slm dry Ar with 1% feed gas admixture of molecular oxygen was determined.

The additional O_2 content in the plasma zone can also explain the reduced effective lifetime of the measurements compared to the calculated lifetimes for the O atom measurements. Considering an additional content of 1% O_2, the calculated effective lifetime is reduced to (1.5 ± 0.1) ns, which is within the error in agreement with the measured values. Since the effective lifetime of excited O atoms was measured for each data point, additional quenching has already been considered. The effective lifetime for excited H atoms will be reduced by O_2 quenching from 90 ps to 85 ps, which is covered by the errorbars of 14 ps.

In Figure 9, the main O and H atom production and consumption mechanisms are shown as a function of the axial distance z. G_O and G_H denote the source terms for O and H atoms respectively, as resulting from the local plasma chemical model. The R_i's are the formation rates of the individual reactions, see Table 3, as obtained from the reacting flow model.

The production and consumption rates for O atoms and for H atoms were highest at

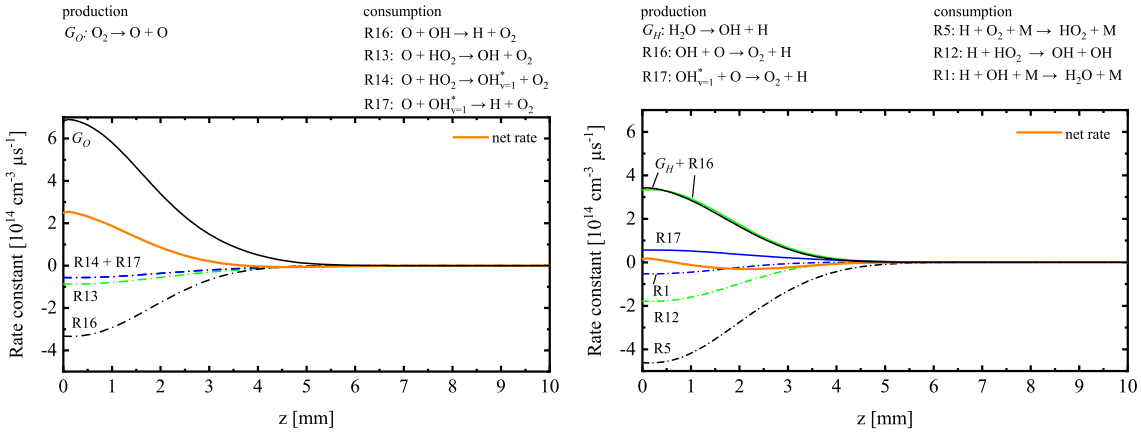

(a) oxygen (b) hydrogen

Figure 9: Production and consumption rates for (a) O atoms and (b) H atoms as a function of the axial distance z from the nozzle.

the nozzle outlet, and decreased to 0 at approximately $z = 5$ mm, as both, O and H atoms, were consumed within the first 5 mm from the nozzle.

The O atom production is dominated by the source term G_O through the dissociation of molecular oxygen by metastable argon atoms and excimers. Although reactions with N_2 were considered in the model (R21 - R39), their impact was negligible, since no N_2 was present in the plasma zone. The O atom consumption is mainly through reactions (R16) and (R17) with OH to form H atoms, and through reactions (R13) and (R14) with HO_2 to form OH radicals. The net formation rate becomes negative at a distance of 3.7 mm from the nozzle., i.e., for larger distances more O atoms are consumed than produced.

By comparison, the H atom formation is not only governed by dissociation of H_2O into OH and H by metastable argon atoms and excimers, but also through reactions (R16) and (R17) of O with OH, which, as mentioned before, are dominant consumption pathway for the O atoms. The H atom consumption is mainly through the three-body reactions with O_2 (R5) and OH (R1), and to some extend through reaction (R12). These three reactions represent at the same time the main life cycle of HO_2, according to Gianella et al. [16]. Starting from $z = 0.6$ mm, the consumption was larger than the production with a maximum loss rate of $-3.1 \cdot 10^{13}$ cm^{-3} µs^{-1} at $z = 2.2$ mm.

The formation of ozone as a stable end product is covered in the plasma chemical and reacting flow model through the three-body reaction (R4) of O with O_2. The corresponding rate, when compared with other O atom consumption pathways, is found to be a factor of 15 lower than the combined rate of the O with HO_2 reactions (R13 - R15), and a factor of about 40 lower than the combined rate of the O with OH reactions (R16 - R18). This is in agreement with the decrease of the ozone net production rate due to humidity admixtures greater than 1000 ppm to the feed gas, as previously reported by Winter et al. [14]; at such humidity admixtures, the consumption of O is dominated by OH and HO_2 rather than by O_2 to form ozone.

This work demonstrates that the densities of the atomic radicals, O and H, and the molecular radicals, OH and HO_2, strongly depend on the molecular oxygen content in the plasma zone and the effluent. It has been shown that even small amounts, approximately 1%, of O_2 in the plasma zone, has a drastic impact on the reactive species composition in the effluent.

6. Conclusion

In this work, the spatial distribution of O and H atoms in the effluent of the CAPJ kINPen-sci was measured with picosecond TALIF. By employing this method, the effective lifetime was determined independently from quenching coefficients in the case of atomic O. Due to high quenching rates, the effective lifetime of H was below the detection limit of the system and was evaluated using reported quenching coefficients. An asymmetry in the radial distributions was observed, where the maximum was found within the region between $x = 0.0$ mm and $x = 0.5$ mm. A maximum O density of $(3.8 \pm 0.7) \cdot 10^{15}$ cm^{-3} and a maximum H density of $(3.5 \pm 1.0) \cdot 10^{15}$ cm^{-3} was determined close to the nozzle, which were reduced below the detection limit within the first 4 mm below the nozzle. It was found that the curtain gas composition has a negligible influence on the atomic O and H density distributions at short distances from the nozzle. Moreover, the gas composition in the plasma zone was observed to play a key role on the formation of O and H atoms. The main production and consumption reactions were determined by comparing the experimental data with a plasma chemical and reacting flow model. 1% O_2 was added to the feed gas in order to match the experimental data with the simulated densities. The origin of this initial amount of molecular oxygen was found to be independent from the gas curtain composition and not a result of impurities in the feed gas. An explanation is given by considering backwards

directed excitation waves, which may lead to a drift of negative oxygen molecules into the plasma zone. O atoms were mainly produced by the dissociation of O_2 within the plasma zone and consumed by OH and HO_2 radicals. H atoms were produced by the dissociation of water in the plasma zone and the reaction of OH with O atoms. Whereas, they were consumed by O_2, HO_2, and OH. The maximum loss rate for H atoms was found at $z = 2.2$ mm; this is close to the point where diffusion of the gas curtain into the effluent starts to become efficient.

This works demonstrates the strong connection between O and H atoms, OH and HO_2 radicals, and O_2 molecules. Even small amounts of about 1% of O_2 in the plasma zone have a high impact on the reactive species composition, whereas the diffusion of surrounding gas into the effluent determines the distribution within the effluent.

7. Acknowledgements

The authors would like to thank Richard Armitage for the technical support and Torsten Gerling for fruitful discussions. The authors would also like to recognise the funding provided by the UK EPSRC through the grant number EP/K018388/1.

References

[1] Laroussi M and Akan T 2007 *Plasma Process. Polym.* **4** 777–788

[2] Penkov O V, Khadem M, Lim W S and Kim D E 2015 *J. Coat. Technol. Res.* **12** 225–235

[3] Fanelli F and Fracassi F 2017 *Surf. Coat. Tech.* **322** 174–201

[4] von Woedtke T, Reuter S, Masur K and Weltmann K D 2013 *Phys. Rep.* **530** 291–320

[5] Fridman A and Friedman G (eds) 2013 *Plasma medicine* (Chichester: John Wiley and Sons Ltd)

[6] Ito M, Oh J S, Ohta T, Shiratani M and Hori M 2017 *Plasma Process. Polym.* **15** e20l700073

[7] Privat-Maldonado A, Schmidt A, Lin A, Weltmann K D, Wende K, Bogaerts A and Bekeschus S 2019 *Oxidative Medicine and Cellular Longevity* **2019** 9062098

[8] Winter J, Brandenburg R and Weltmann K D 2015 *Plasma Sources Sci. Technol.* **24** 064001

[9] Weltmann K D and von Woedkte T 2017 *Plasma Phys. Control. Fusion* **59** 014031

[10] Keidar M 2015 *Plasma Sources Sci. Technol.* **24** 033001

[11] Jablonowski H and von Woedtke T 2015 *Clinical Plasma medicine* **3** 42–52

[12] von Woedtke T, Metelmann H R and Weltmann K D 2014 *Contrib. Plasma Phys.* **54** 104 – 117

[13] Graves D B 2012 *J. Phys. D: Appl. Phys* **45** 263001

[14] Winter J, Wende K, Masur K, Iseni S, Dünnbier M, Hammer M U, Tresp H, Weltmann K D and Reuter S 2013 *J. Phys. D: Appl. Phys.* **46** 295401

[15] Ikawa S, Kitano K and Hamaguchi S 2010 *Plasma Process. Polym.* **7** 33–42

[16] Gianella M, Reuter S, Press S A, Schmidt-Bleker A, van Helden J P H and Ritchie G A D 2018 *Plasma Sources Sci. Technol.* **27** 095013

[17] Schmidt-Bleker A, Winter J, Bösel A, Reuter S and Weltmann K D 2016 *Plasma Sources Sci. Technol.* **25** 015005

[18] Wende K, von Woedtke T, Weltmann K D and Bekeschus S 2018 *Biological Chemistry* **400** 1437–4315

[19] Reuter S, Sousa J S, Stancu G D and van Helden J P H 2015 *Plasma Sources Sci. Technol.* **24** 054001

[20] Niemi K, O'Connell D, de Oliveira N, Joyeux D, Nahon L, Booth J P and Gans T 2013 *Appl. Phys. Lett.* **103** 034102

[21] Dedrick J, Schröter S, Niemi K, Wijaikhum A, Wagenaars E, de Oliveira N, Nahon L, Booth J P, O'Connell D and Gans T 2017 *J. Phys. D: Appl. Phys.* **50** 455204

[22] Peverall R and Ritchie G A D 2019 *Plasma Sources Sci. Technol.* **28** 073002

[23] Yue Y, Kondeti V S S K and Bruggeman P J 2020 *Plasma Sources Sci. Technol.* **29** 04LT01

[24] Schmidt J B, Sands B L, Kulatilaka W D, Roy S, Scofield J and Gord J R 2015 *Plasma Sources Sci. Technol.* **24** 032004

[25] Reuter S, Winter J, Schmidt-Bleker A, Schroeder D, Lange H, Knake N, von der Gathen V S and Weltmann K D 2012 *Plasma Sources Sci. Technol.* **21** 024005

[26] Yatom S, Luo Y, Xiong Q and Bruggeman P J 2017 *J. Phys. D: Appl. Phys.* **50** 415204

[27] Schröter S, Bredin J, Gibson A R, West A, Dedrick J P, Wagenaars E, Niemi K, Gans T and O'Connell D 2020 *arxive.org*

[28] Niemi K, von der Gathen V S and Döbele H F 2001 *J. Phys. D: Appl. Phys.* **34** 2330

[29] Niemi K, von der Gathen V S and Döbele H F 2005 *Plasma Sources Sci. Technol.* **14** 375

[30] Reuter S, von Woedtke T and Weltmann K D 2018 *J. Phys. D: Appl. Phys.* **51** 233001

[31] Gerling T, Brandenburg R, Wilke C and Weltmann K D 2017 *Eur. Phys. J. Appl. Phys.* **78** 10801

[32] Reuter S, Winter J, Schmidt-Bleker A, Tresp H, Kammer M U and Weltmann K D 2012 *IEEE Transactions on plasma science* **40** 2788–2794

[33] Goehlich A, Kawetzki T and Döbele H F 1998 *J. Chem. Phys.* **108** 9362

[34] Schmidt J B, Roy S, Kulatilaka W D, Shkurenkov I, Adamovich I V, Lempert W R and Gord J R 2017 *J. Phys. D: Appl. Phys.* **50** 015204

[35] Bittner J, Kohse-Höinghaus K, Meier U and Just T 1988 *Chemical Physics Letters* **143** 571–576

[36] West A T 2016 *Optical and Electrical Diagnosis of Atmospheric Pressure Plasma Jets* Ph.D. thesis University of York

[37] Semenov I L and Weltmann K D 2020 *Plasma Sources Sci. Technol.* **29** 055001

[38] Hagelaar G and Pitchford L 2005 *Plasma Sources Sci. Technol.* **14** 722–33

[39] Van Gaens W and Bogaerts A 2013 *J. Phys. D: Appl. Phys.* **46** 275201

[40] Fu Y, Krek J, Parsey G M and Verboncoeur J P 2018 *Phys. Plasmas* **25** 033505

[41] Keto J W, Gleason Jr R and Walters G 1974 *Phys. Rev. Lett.* **33** 1365

[42] Mehnert R, Brede O and Hermann R 1986 *Int. J. Radiat. Appl. Instrum.: Part C Radiat. Phys. Chem.* **28** 455–60

[43] Piper L, Velazco J and Setser D 1973 *J. Chem. Phys.* **59** 3323–40

[44] Novicki S and Krenos J 1988 *J. Chem. Phys.* **89** 7031–3

[45] Keto J W, Hart C and Kuo C Y 1981 *J. Chem. Phys.* **74** 4450–4

[46] Reuter S, Winter J, Iseni S, Peters S, Schmidt-Bleker A, Dünnbier M, Schäfer J, Foest R and Weltmann K 2012 *Plasma Sources Sci. Technol.* **21** 034015

[47] Hübner S, Hofmann S, Van Veldhuizen E and Bruggeman P 2013 *Plasma Sources Sci. Technol.* **22** 065011

[48] Van Gaens W, Bruggeman P J and Bogaerts A 2014 *New J. Phys.* **16** 063054

[49] Baulch D, Cobos C, Cox R, Esser C, Frank P, Just T, Kerr J, Pilling M, Troe J, Walker R *et al.* 1992 *J. Phys. Chem. Ref. Data* **21** 411–734

[50] Tsang W and Hampson R 1986 *J. Phys. Chem. Ref. Data* **15** 1087–279

[51] Atkinson R, Baulch D, Cox R, Hampson Jr R, Kerr J, Rossi M and Troe J 1997 *J. Phys. Chem. Ref. Data* **26** 521–1011

[52] Michael J, Su M C, Sutherland J, Carroll J and Wagner A 2002 *J. Phys. Chem. A* **106** 5297–313

[53] Atkinson R, Baulch D, Cox R, Crowley J, Hampson R, Hynes R, Jenkin M, Rossi M and Troe J 2004 *Atmospheric Chem. Phys.* **4** 1461–738

[54] Makhlouf U, Picard R and Winick J 1995 *J. Geophys. Res.* **100** 11289–311

[55] Thrush B and Wilkinson J 1981 *Chemical Physics Letters* **81** 1–3

[56] Kossyi I, Kostinsky A Y, Matveyev A and Silakov V 1992 *Plasma Sources Sci. Technol.* **1** 207–20

[57] Herron J T 1999 *J. Phys. Chem. Ref. Data* **28** 1453–83

[58] Atkinson R, Baulch D, Cox R, Hampson Jr R F, Kerr J and Troe J 1989 *J. Phys. Chem. Ref. Data* **18** 881–1097

[59] DeMore W, Sander S, Golden D, Hampson R, Kurylo M, Howard C, Ravishankara A, Kolb C and Molina M 1997 *JPL Publication 97-4: Chemical Kinetics and Photochemical Data for Use in Stratospheric Modeling* (Pasadena, California: Jet Propulsion Laboratory, California Institute of Technology)

[60] Campbell I and Gray C 1973 *Chem. Phys. Lett.* **18** 607–9

[61] Tsang W and Herron J T 1991 *J. Phys. Chem. Ref. Data* **20** 609–63

[62] Boodaghians R B, Canosa-Mas C E, Carpenter P J and Wayne R P 1988 *J. Chem. Soc. Faraday Trans.* **84** 931–48

[63] Klose S J, Manfred K M, Norman H C, Ritchie G A D and van Helden J H 2020 *Plasma Sources Sci. Technol.*

[64] Iseni S, Schmidt-Bleker A, Winter J, Weltmann K D and Reuter S 2014 *J. Phys. D: Appl. Phys.* **47** 152001

[65] Dünnbier M, Schmidt-Bleker A, Winter J, Wolfram M, Hippler R, Weltmann K D and Reuter S 2013 *J. Phys. D: Appl. Phys.* **46** 435203

[66] Schmidt-Bleker A, Norberg S A, Winter J, Johnsen E, Reuter S, Weltmann K D and Kushner M J 2015 *Plasma Sources Sci. Technol.* **24** 035022

[67] Reuter S, Winter J, Iseni S, Peters S, Schmidt-Bleker A, Dünnbier M, Schäfer J, Foest R and Weltmann K D 2012 *Plasma Sources Sci. Technol.* **21** 034015

Table 3: List of reactions used in the reacting flow model.

R1	$H + OH + M \rightarrow H_2O + M$	2.56×10^{-31}	[49]
R2	$H + O + M \rightarrow OH + M$	4.33×10^{-32}	[50]
R3	$H + H + M \rightarrow H_2 + M$	6.00×10^{-33}	[49]
R4	$O + O_2 + M \rightarrow O_3 + M$	5.90×10^{-34}	[51]
R5	$H + O_2 + M \rightarrow HO_2 + M$	2.12×10^{-32}	[52]
R6	$HO_2 + HO_2 \rightarrow H_2O_2 + O_2$	1.63×10^{-12}	[53]
R7	$HO_2 + HO_2 + M \rightarrow H_2O_2 + O_2 + M$	4.98×10^{-32}	[53]
R8	$OH + OH + M \rightarrow H_2O_2 + M$	6.86×10^{-31}	[51]
R9	$OH + OH \rightarrow O + H_2O$	1.87×10^{-12}	[51]
R10	$H + HO_2 \rightarrow H_2 + O_2$	6.66×10^{-12}	[49]
R11	$H + HO_2 \rightarrow H_2O + O$	2.79×10^{-12}	[49]
R12	$H + HO_2 \rightarrow OH + OH$	6.46×10^{-11}	[49]
R13	$O + HO_2 \rightarrow OH + O_2$	3.01×10^{-11}	[53, 54]
R14	$O + HO_2 \rightarrow OH^*_{v=1} + O_2$	1.97×10^{-11}	[53, 54]
R15	$O + HO_2 \rightarrow OH^*_{v=2} + O_2$	7.54×10^{-12}	[53, 54]
R16	$OH + O \rightarrow H + O_2$	3.90×10^{-11}	[54]
R17	$OH^*_{v=1} + O \rightarrow H + O_2$	1.00×10^{-10}	[54]
R18	$OH^*_{v=2} + O \rightarrow H + O_2$	2.50×10^{-10}	[54]
R19	$OH + H_2O_2 \rightarrow HO_2 + H_2O$	1.70×10^{-12}	[53]
R20	$OH + HO_2 \rightarrow H_2O + O_2$	5.80×10^{-11}	[55]
R21	$N^*_2 + O \rightarrow NO + N$	7.00×10^{-12}	[56]
R22	$N^*_2 + O_2 \rightarrow N_2 + O + O$	2.54×10^{-12}	[56]
R23	$N^*_2 + O_2 \rightarrow N_2 + O^*_2$	1.30×10^{-12}	[56]
R24	$O^*_2 + N^*_2 \rightarrow N_2 + O + O$	2.00×10^{-11}	[57]
R25	$N + OH \rightarrow NO + H$	5.05×10^{-11}	[58]
R26	$N + NO \rightarrow N_2 + O$	2.92×10^{-11}	[59]
R27	$O + NO + M \rightarrow NO_2 + M$	9.90×10^{-32}	[51]
R28	$O + NO_2 + M \rightarrow NO_3 + M$	8.90×10^{-32}	[51]
R29	$O + NO_2 \rightarrow NO + O_2$	1.03×10^{-11}	[53]
R30	$O + NO_3 \rightarrow NO_2 + O_2$	1.70×10^{-11}	[53]
R31	$N + O + M \rightarrow NO + M$	9.16×10^{-33}	[60]
R32	$H + NO + M \rightarrow HNO + M$	3.86×10^{-32}	[61]
R33	$H + NO_2 \rightarrow OH + NO$	1.40×10^{-10}	[61]
R34	$H + NO_3 \rightarrow OH + NO_2$	1.10×10^{-10}	[62]
R35	$O + HNO \rightarrow OH + NO$	5.99×10^{-11}	[61]
R36	$OH + NO + M \rightarrow HNO_2 + M$	6.88×10^{-31}	[59]
R37	$OH + NO_2 + M \rightarrow HNO_3 + M$	2.60×10^{-30}	[51]
R38	$OH + NO_3 \rightarrow HO_2 + NO_2$	2.00×10^{-11}	[53]
R39	$OH + HNO_2 \rightarrow H_2O + NO_2$	5.01×10^{-12}	[61]

[a] M denotes a third body (the concentration of M is $2.44 \times 10^{19}\,\mathrm{cm}^{-3}$).